Hydration-induced spin-glass state in a frustrated Na-Mn-O triangular lattice

Ioanna Bakaimi,[1,2] Rosaria Brescia,[3] Craig M. Brown,[4,5] Alexander A. Tsirlin,[6] Mark A. Green,[7] and Alexandros Lappas[1,*]

[1]*Institute of Electronic Structure and Laser, Foundation for Research and Technology–Hellas, Vassilika Vouton, 71110 Heraklion, Greece*

[2]*Department of Physics, University of Crete, Voutes, 71003 Heraklion, Greece*

[3]*Nanochemistry Department, Istituto Italiano di Tecnologia, Via Morego 30, 16163 Genova, Italy*

[4]*NIST Center for Neutron Research, 100 Bureau Drive, Gaithersburg, Maryland 20899-8562, USA*

[5]*Department of Chemical and Biomolecular Engineering, University of Delaware, Newark, Delaware 19716, USA*

[6]*Experimental Physics VI, Center for Electronic Correlations and Magnetism, Institute of Physics, University of Augsburg, 86135 Augsburg, Germany*

[7]*School of Physical Sciences, University of Kent Canterbury, Kent CT2 7NH, United Kingdom*

(Received 4 December 2015; published 18 May 2016)

Birnessite compounds are stable across a wide range of compositions that produces a remarkable diversity in their physical, electrochemical, and functional properties. These are hydrated analogs of the magnetically frustrated, mixed-valent manganese oxide structures, with general formula, Na_xMnO_2. Here we demonstrate that the direct hydration of layered rock-salt type α-$NaMnO_2$, with the geometrically frustrated triangular lattice topology, yields the birnessite type oxide, $Na_{0.36}MnO_2 \cdot 0.2H_2O$, transforming its magnetic properties. This compound has a much-expanded interlayer spacing compared to its parent α-$NaMnO_2$ compound. We show that while the parent α-$NaMnO_2$ possesses a Néel temperature of 45 K as a result of broken symmetry in the Mn^{3+} sublattice, the hydrated derivative undergoes collective spin freezing at 29 K within the Mn^{3+}/Mn^{4+} sublattice. Scaling-law analysis of the frequency dispersion of the ac susceptibility, as well as the temperature-dependent, low-field dc magnetization confirm a cooperative spin-glass state of strongly interacting spins. This is supported by complementary spectroscopic analysis [high-angle annular dark-field scanning transmission electron miscroscopy (TEM), energy-dispersive x-ray spectroscopy, and electron energy-loss spectroscopy] as well as by a structural investigation (high-resolution TEM, x-ray, and neutron powder diffraction) that yield insights into the chemical and atomic structure modifications. We conclude that the spin-glass state in birnessite is driven by the spin frustration imposed by the underlying triangular lattice topology that is further enhanced by the in-plane bond-disorder generated by the mixed-valent character of manganese in the layers.

DOI: 10.1103/PhysRevB.93.184422

I. INTRODUCTION

Layered manganese oxides containing triangular magnetic lattice topology have demonstrated important phenomena, including magnetic frustration [1], unique electronic properties as a result of Jahn-Teller active Mn^{3+} cations [2], and the development of different polymorphic phases [3] with variable magnetic response and redox potentials, overall reflecting a notable interplay between microstructure and properties. Due to their modular porosities, high thermal surface area, and stabilities, these compounds find numerous technological applications such as their use in ion sieves, molecular sieves, catalysts [4,5], and electrodes in batteries. One of the most prominent characteristics of manganese oxides is that their structure can be used as a host material for intercalation and deintercalation reactions. $LiMnO_2$ [6] is a member of the manganese oxides family, which is widely known for its use as cathode material in Li rechargeable batteries. The replacement of the conventional Li-based compounds with Na-based ones, such as birnessite, is of great importance due to the higher abundance and relative low cost of sodium compared with lithium. Examples of sodium manganese oxides which have been studied as candidates for the aforementioned applications are the $Na_{0.44}MnO_2$ [6,7] and the β-$NaMnO_2$ [8]. Especially interesting is the latter, where tuning the concentration of planar defects [3] determines its quality as a high-performance cathode material for battery technologies [9].

A common characteristic of layered manganese oxides is the presence of edge shared MnO_6 octahedral units, which are separated by metal ions such as Li, Na, or K [10]. The interlayer distance varies between particular structures from ∼4.7 Å in $Li_{1.09}Mn_{0.91}O_2$ [11] to ∼7 Å in the birnessite [12] and ∼10 Å in the buserite structure [13]. The hydrated $NaMnO_2$ oxides, whose Na/Mn molar ratio is between 0.2 and 0.7, are known as Na-birnessites [10,14]. Depending on the intercalating cation, there are also K-, Li- [15], Bi-, or Zn-based birnessites. The latter have recently been discussed to have a critical role in Zn batteries during the charging process [16]. Interestingly, a recent study showed that hydrated manganese oxides, such as $Na_{0.71}MnO_2 \cdot 0.25H_2O$, have superior cycling stability and high capacity as a result of the presence of water within the interlayer gap [17].

There are several studies [11,12,15,18–20] describing the preparation methods of birnessites including deintercalation [19], ion exchange [19], and hydrothermal synthesis [18]. Here, we evaluate Na-birnessite prepared from direct hydration of pure geometrically frustrated α-$NaMnO_2$. The latter is a rock-salt-type derivative (C2/m, $a = 5.67$ Å, $b = 2.85$ Å, $c = 5.80$ Å, $\beta = 113.2^\circ$) which may be used as a precursor for the preparation of the cathode material $LiMnO_2$. Its structure is composed of sheets of edge-sharing MnO_6 octahedra, which are separated by a single two-dimensional layer of Na cations. Geometric magnetic frustration develops as the Jahn-Teller (J-

*lappas@iesl.forth.gr

T) active Mn^{3+} ($3d^4$, $S = 2$) distorts the in-plane Mn-topology, allowing for a spatially anisotropic J_1-J_2 two-dimensional (2D) triangular spin lattice [1]. When spin frustration is lifted below 45 K, this system adopts a remarkable nanoscale inhomogeneity in the ground state, with Néel order being the outcome of local symmetry-breaking pinning sites [21]. A recent study highlights that the formation of different $NaMnO_2$ polymorphs, such as α-$NaMnO_2$ and β-$NaMnO_2$, is largely driven by the evolution of relative concentration of planar defects in their microstructure [3]. Moreover, alkali substoichiometry, as in α-$Na_{0.7}MnO_{2.25}$ [22], allows mixing of Mn^{3+} and Mn^{4+} states, therefore determining the important role of structural details in modifying the cooperative nature of the electronic/magnetic properties. The latter is demonstrated in a spectacular manner with the interplay of Na vacancies and cooperative J-T effects in $Na_{5/8}MnO_2$ [23], where a favorable charge-ordered state is established. However, despite the plethora of synthesis-based studies found in the literature, there are only few reports related to the magnetic properties of birnessite-based systems [24]. One such study is the reported work on birnessite-type MnO_2 nanowalls [24] that were found to exhibit a magnetic transition at 9.2 K, evident by a bifurcation of the dc susceptibility zero field-cooled (ZFC) and field-cooled (FC) curves. The magnetic properties of the birnessite type nanowalls were attributed to the antiferromagnetic interactions between the Mn^{3+}/Mn^{4+} cations [24].

In this work, we examine the impact of the structure and composition modifications on the magnetism after intercalating water molecules between the MnO_6 layers of α-$NaMnO_2$. The hydration of the latter resulted in the formation of birnessite-type material with the composition $Na_{0.36}MnO_2 \cdot 0.2H_2O$ and concomitant enhancement of the interlayer spacing. This drastically changes the magnetic properties and the antiferromagnetic ordering of the parent α-$NaMnO_2$ gives way to a strongly interacting spin-glass state. Indeed, extensive dc and ac magnetic susceptibility studies corroborate that the system undergoes spin-glass freezing below 29 K. We demonstrate that the frequency dispersion of the temperature-dependent ac susceptibility maximum is described well on the basis of the dynamic scaling theory, entailing a phenomenological power-law behavior. Based on the experimental evidence we discuss that frustration caused by bond disorder, attributed to competing exchange interactions due to random distribution of the Mn^{3+}/Mn^{4+} cations, provides the conditions for such an emerging state.

II. EXPERIMENTAL PROCEDURES

Polycrystalline powder of $Na_{0.36}MnO_2 \cdot 0.2H_2O$ (hereafter referred to as Na-birnessite) was synthesized by direct hydration of α-$NaMnO_2$ [1] and based on a synthesis protocol previously reported [25]. The starting material α-$NaMnO_2$ was prepared by solid-state reaction: Stoichiometric amounts of Na_2CO_3 and Mn_2O_3 were mixed, ground, pelletized, and heated from room temperature up to 750 °C, with a heating rate of 3 °C/ min under an argon atmosphere [3]. After holding at high temperature for 60 h the pellet was cooled to room temperature. The final product was exposed to ambient atmosphere for 2 weeks. This ensured the homogeneous hydration of α-$NaMnO_2$ within the interlayer gaps, which leads to the formation of the Na-birnessite compound. Frequent mixing of the powder was undertaken so all crystallites would become exposed to air. This promoted the homogeneity of the final compound, while the powder converted from the host framework α-$NaMnO_2$ to the Na-birnessite.

x-Ray powder diffraction (XRPD) experiments were carried out on a Rigaku [26] D/MAX-2000H rotating Cu anode diffractometer ($\lambda = 1.5406$ Å). Samples were prepared for Transmission electron microscopy (TEM) investigations by mild sonication in ethanol and drop-casting onto Cu grids covered with a holey carbon film. High-resolution transmission electron microscopy (HRTEM), electron energy-loss spectroscopy (EELS), and energy-dispersive x-ray spectroscopy (EDS) analyses were carried out using a Jeol JEM 2200FS instrument, equipped with a Schottky emitter operated at 200 kV, a CEOS spherical aberration corrector of the objective lens allowing for a spatial resolution of 0.9 Å, and an in-column imaging filter (Ω type). EELS analyses were carried out in TEM mode (convergence and collection angles 5.5 and 1 mrad, respectively, 0.4 eV/pixel dispersion) and the quantification was carried out by using the software "EELS Model" [27]. EDS mapping and compositional quantification were determined in scanning TEM (STEM) high-angle annular dark-field (HAADF) imaging mode, using a Bruker Quantax 400 system with a 60-mm^2 XFlash 5060 silicon drift detector. Thermal analysis [thermogravimetric (TGA) and differential thermal analysis (DTA)] was performed on a SDT-Q600 TA instruments system under Ar-gas flow. Neutron powder diffraction (NPD) data were collected using the high-resolution powder diffractometer BT-1 at the National Institute of Standards and Technology Center for Neutron Research (NCNR), with a wavelength of 1.5406 Å and 60′ collimation from the Cu-311 monochromator.

Magnetic susceptibility (dc and ac) was measured on a Superconducting Quantum Interference Device (SQUID) magnetometer (Quantum Design MPMS-XL5) under various protocols and magnetic fields ($H = 2.5$–100 mT). The frequency dependent ($f = 47$–901 Hz) ac susceptibility data, which were analyzed by appropriate phenomenological laws, were collected using the temperature sweep mode of the MPMS. This mode was chosen as a more appropriate one, since it affects less the thermodynamic and time-dependent phenomenon of the encountered spin-glass transition.

III. RESULTS AND DISCUSSION

A. Transmission electron microscopy studies (EDS, HRTEM, EELS)

EDS quantification has been performed in STEM mode by the Cliff-Lorimer method, combined with HAADF-STEM imaging to determine the distribution of the Na, Mn, and O atoms in the Na-birnessite sample. While EDS mapping typically shows a homogeneous distribution of Mn, O, and Na over individual crystals (Fig. 1), atomic quantification over several crystals results in an average Na/Mn ratio of 0.36(±0.10). Due to the low accuracy of EDS for quantification of light elements, the O/Mn atomic ratio was instead obtained as 2.2(±0.5) from EELS analyses over three different crystals of Na-birnessite. According to elemental analyses, the chemical

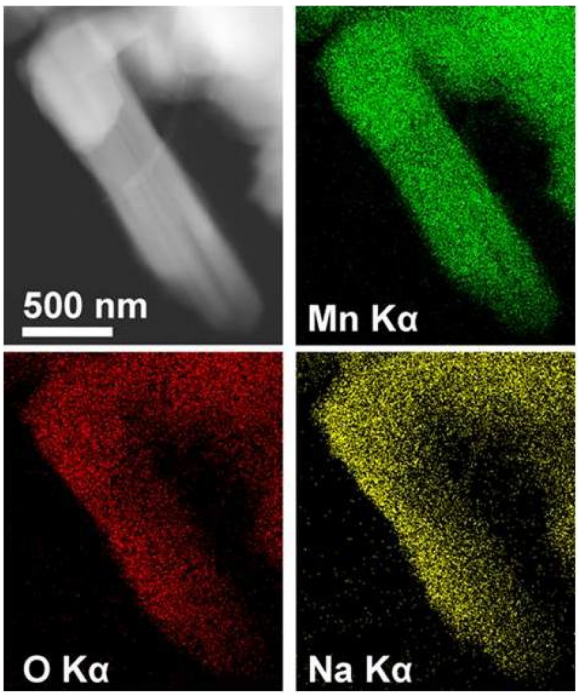

FIG. 1. HAADF-STEM image of a typical Na-birnessite crystal and corresponding EDS maps showing the homogeneous distribution of Mn, Na, and O over it.

formula corresponding to the hydrated compound was then estimated to be $Na_{0.36}MnO_2 \cdot 0.2H_2O$.

Together with the aforementioned results of compositional analysis, a HRTEM study of individual crystallites was fundamental for the identification of the crystal structure of the Na birnessite phase. The images reveal the presence of μm-scale crystals in the hydrated compound whose structure matched well that reported for $Na_{0.3}MnO_2 \cdot 0.93H_2O$ [28] birnessite. Figure 2 (and Fig. S1) presents one such crystal which has been used for the analysis. The fast Fourier transform

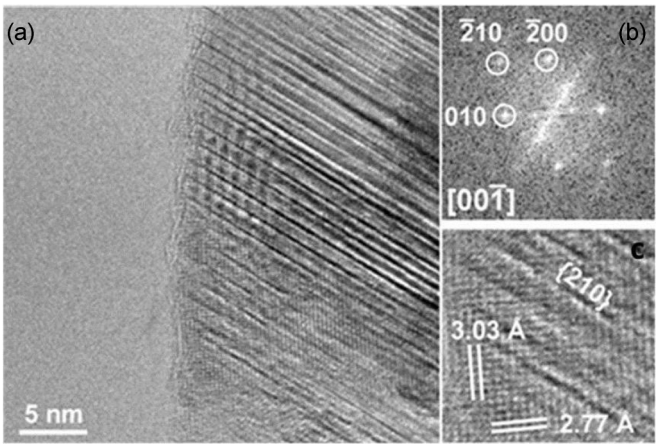

FIG. 2. (a) HRTEM image of a typical crystallite in the Na-birnessite sample, suspended in vacuum and (b) fast Fourier transform (FFT) of the area in (c). The observed diffraction spot-pattern matches the [00$\bar{1}$]-oriented triclinic $Na_{0.3}MnO_2 \cdot 0.93H_2O$ lattice, with 6% cell expansion.

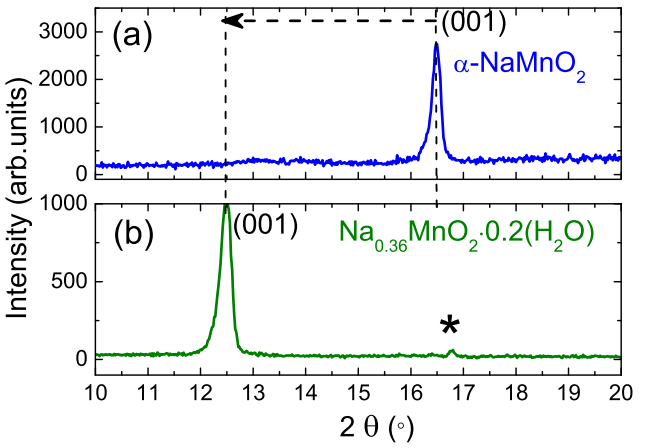

FIG. 3. Low-angle part of the XRPD patterns for α-$NaMnO_2$ (a) and the Na-birnessite (b), showing the characteristic shift of the 001 Bragg reflection upon hydration; (*), nonconverted parent α-$NaMnO_2$.

[FFT; Fig. 2(b)] of the area in Fig. 2(c) matches the [00$\bar{1}$] orientation of the $Na_{0.3}MnO_2 \cdot 0.93H_2O$ phase, with a 6% dilation compared to the reported cell parameters. According to the FFT, analysis the hydrated compound crystallizes in the triclinic system (space group C$\bar{1}$), with the following cell parameters: $a = 5.53(1)$ Å, $b = 3.11(6)$ Å, $c = 7.80(1)$ Å, $\alpha = 89.492(13)^\circ$, $\beta = 103.136(12)^\circ$, $\gamma = 89.929(10)^\circ$. Stacking faults appear parallel to the {210} planes [Fig. 2(c)]. These structural defects are not parallel to the {100} planes, in which H_2O molecules are inserted in the structure. The structural modifications could result from Mn vacancies. Noticeably, the c parameter has increased in the hydrated final product by $\sim$2 Å in comparison with that of the parent host α-$NaMnO_2$ ($c \sim 5.8$ Å, at room temperature). This is nicely illustrated by means of XRPD (Fig. 3), in which the 001 Bragg reflection of α-$NaMnO_2$ is shifted towards lower angles when the Na-birnessite compound is formed. A schematic representation of the ideal structure shown in Fig. 4 depicts the hydrated material's in-plane triangular Mn sublattice topology.

Furthermore, the manganese $L_{2,3}$ core-loss EEL spectrum of Na-birnessite was recorded (Fig. S2) and carefully analyzed based on the white-line ratio method [29]. According to this method, the integral intensity ratio of the L_3 and L_2 excitation peaks of a transition metal is correlated to its formal oxidation state [29–35]. The analysis resulted in the average oxidation state of 3.4, postulating a mixed valent (Mn^{3+}/Mn^{4+}) character for the manganese cations.

B. Thermogravimetric analysis

Measurements of the weight-loss versus temperature were carried out from room temperature up to 1100 °C with a small quantity (<10 mg) of the Na-birnessite sample that was heated up with a constant rate of 20 °C/ min. The results are shown in Fig. 5. Above 100 °C there is a 13% decrease in the weight up to 500 °C, which is attributed to the removal of H_2O from the Mn-O sheets. Correspondingly the DTA graph exhibits a sharp endothermic peak around 140 °C due to the dehydration of Na-birnessite. Further heating between 500 and 800 °C

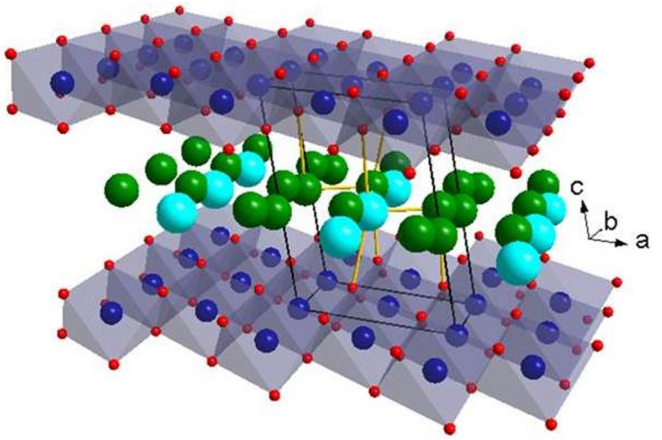

FIG. 4. Schematic representation of the crystal structure of the Na-birnessite: the manganese, oxygen, sodium atoms are represented with the blue, red and green spheres; the H_2O molecules in the interlayer space are shown with the turquoise spheres; cell edges are represented with the black lines. For ease of visualization, Na atoms and H_2O molecules, occupying identical positions in the reported structure, are displayed in alternating positions in the model (ICSD 262208).

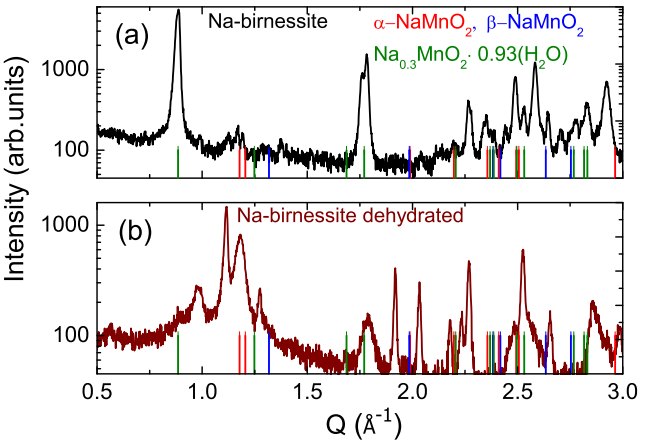

FIG. 6. Comparison of the XRPD patterns of the $Na_{0.3}MnO_2 \cdot 0.2H_2O$ birnessite's polycrystalline powder (a) and the dehydrated compound (b) taken after the TGA experiment performed up to 1100 °C. Indexing of the reflections has been done on the basis of the α-$NaMnO_2$ (ICSD 16270), β-$NaMnO_2$ (ICSD 16271) and the $Na_{0.3}MnO_2 \cdot 0.93H_2O$ (ICSD 262208) phases, whose Bragg reflections are indicated with red, blue and green tick marks, respectively. Bragg peaks attributed to the Mn_3O_4 (ICSD 68174, ICSD 1514104) are left without tick marks for ease of comparison.

results in about 4% reduction of the compound's weight that is accompanied by a broad dip in the DTA curve, which starts above 400 °C and an endothermic peak at 642 °C. The changes in this temperature regime may be caused by a transformation of birnessite to other layered polymorphs such as γ-MnO_2, and its subsequent partial conversion to Mn_2O_3, inferring reduction of the tetravalent manganese correlated also with the release of oxygen [18]. Due to the disproportionation of manganese valence state, analogous observations have been made in the TGA-DTA measurements for Na-deficient α-$Na_{0.7}MnO_{2.25}$ [22], as well as other birnessite-like systems, including ($H_{0.22}MnO_2 \cdot 0.62H_2O$) [36] and $Na_4Mn_{14}O_{27}$ $9H_2O$ [14]. The additional weight loss (∼2%) up to 1000 °C likely relates to redox/extraction reactions due to the increased mobility of alkali ions in forming high-temperature manganese polymorphs. In view of this, powder XRD was performed

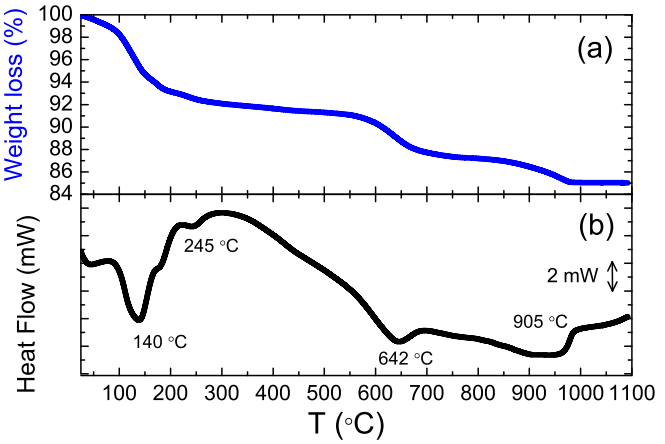

FIG. 5. (a) Thermogravimetric (TGA) and (b) heat-flow (DTA) measurements for the Na-birnessite up to 1100 °C.

on the product formed immediately after the TGA-DTA experiment and compared to the as-synthesized compound. The XRPD patterns presented in Fig. 6 indicate that the sample heated up to 1100 °C in the TGA reverts back to layered α-$NaMnO_2$, although impurities of β-$NaMnO_2$ and Mn_3O_4 phases are also present. The absence of the (001) reflection in Na-birnessite after the heating stage confirms the elimination of intercalated H_2O in the final product.

C. Neutron powder diffraction

NPD patterns were taken at different temperatures, namely at 5, 20, 50, and 300 K (Fig. 7), with the purpose to identify any possible phase transitions of either structural or magnetic origin. Although the high background due to the large incoherent scattering cross section of water protons may hinder low-angle diffuse scattering that would point to short-range or low-dimensional spin correlations, it is important to note the lack of any additional magnetic Bragg scattering in the low-temperature patterns at 5 K and 20 K. This qualitative observation substantiates the absence of long-range magnetic order, confirming that Na-birnessite features a magnetically disordered ground state, presumably stemming from spin frustration caused by competing exchange interactions due to topology and/or site disorder. This is in contrast to the low-angle magnetic Bragg reflections revealed in Na-deficient Na_xMnO_2 ($x = 5/8$), where charge-ordering of Na and Mn stripes yield a fascinating low-temperature magnetic ordering below about 60 K [23].

D. Static magnetic susceptibility

Na-birnessite is synthesized through chemical transformation of the α-$NaMnO_2$ host framework. Our studies provide new evidence for the substantial changes in the magnetic

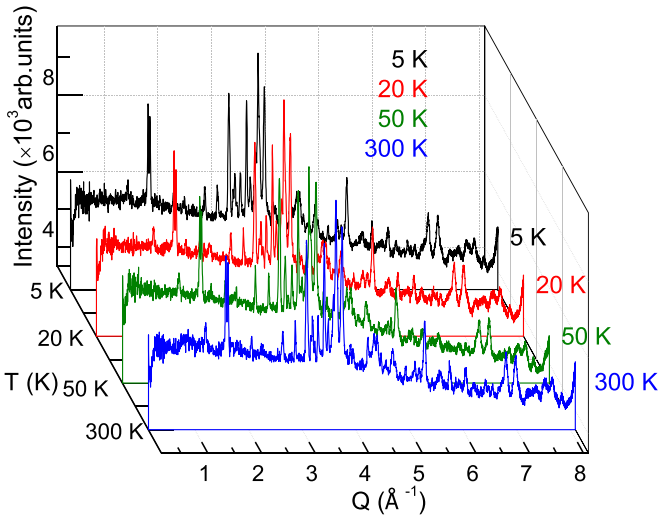

FIG. 7. A series of neutron powder diffraction patterns for Na-birnessite obtained at 5, 20, 50, and 300 K. The absence of reflections of magnetic origin in the low-temperature region, indicates that no long-range magnetic order develops below 29 K.

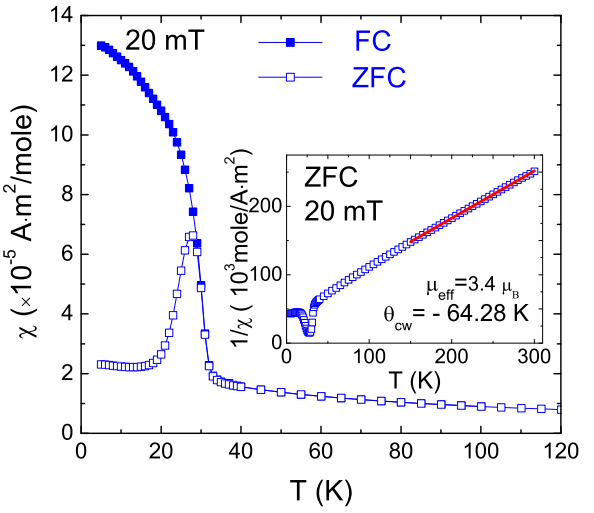

FIG. 9. Low-temperature evolution of the ZFC-FC dc susceptibilities for the Na-birnessite. Note: Characteristic sharp peak at $T_f = 29$ K in the ZFC protocol and bifurcation between the ZFC and FC curves below the T_f. Inset: Curie-Weiss fit (red continuous line) of the reciprocal susceptibility (blue data points).

properties of α-$NaMnO_2$ when converted to Na-birnessite. Figure 8 compares the ZFC dc susceptibility (20 mT) for the two materials. The magnetic susceptibility of α-$NaMnO_2$ does not show a distinct magnetic transition and, instead, a broad hump at high temperatures indicative of low-dimensional magnetism is seen [37]. On the contrary, the magnetic susceptibility of Na-birnessite shows a sharp peak at 29 K, strongly suggesting that the compound undergoes a magnetic transition. We note that in the $AMnO_2$ rock-salt type related derivatives, solid-state nuclear magnetic resonance has shown that the orbital overlap and charge transfer from Mn^{3+} to the interlayer cations ($A = Cu, Na$) is much larger in $CuMnO_2$ than in $NaMnO_2$ [38]. This corroborates to the role of interlayer species controlling the Néel state, setting in at 45 K for Na and at 65 K for Cu, however, accompanied by

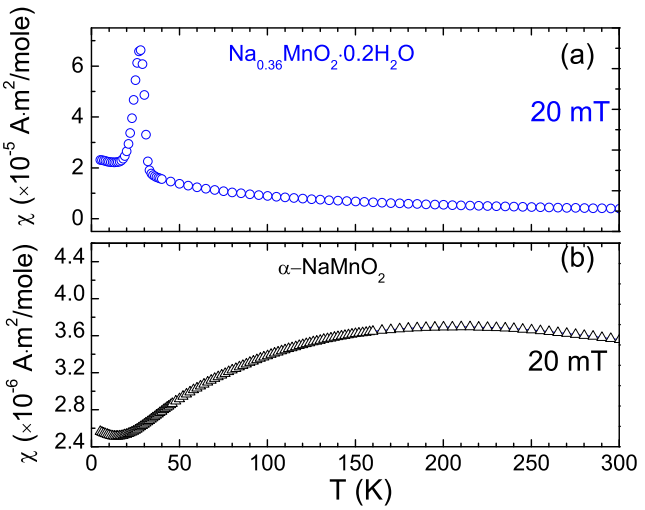

FIG. 8. The temperature evolution of the zero-field cooled (ZFC) dc magnetic susceptibility for (a) α-$NaMnO_2$ and (b) Na-birnessite, under an applied field of 20 mT.

a differing ferromagnetic (FM) and antiferromagnetic (AFM) modification of the Mn-Mn interplane couplings, respectively. In view of these facts, the qualitatively different features in $\chi(T)$ and the nature of the magnetism in α-$NaMnO_2$ and Na-birnessite may be related to the critical modification of the interlayer Mn-Mn interaction strength along the c-axis, stemming from the different nature of the interlayer motifs accommodated therein. Furthermore, the static (dc) magnetic susceptibility of Na-birnessite has been measured on the basis of a ZFC-FC protocol and under a 20-mT external magnetic field (Fig. 9). Below 29 K there is a significant bifurcation between ZFC and FC curves that seems to infer a collective spin freezing, and no long-range magnetic ordered state, in accord with the absence of magnetic Bragg peaks verified by NPD below this transition point. It is worth noting that many compounds which undergo a spin-glass transition, such as the $La_{0.5}Sr_{0.5}CoO_3$ [39], $CuFe_{0.5}V_{0.5}O_2$ [40], $Co_{1-x}Mn_xCl_2 \cdot H_2O$ [41], and, most importantly, the archetypal spin-glass CuMn [42] lack long-range magnetic order but exhibit both the sharp maximum in the ZFC susceptibility, $\chi_{ZFC}(T)$, as well as the divergence between the ZFC and FC curves below the T_f (where T_f stands for the spin-freezing temperature). In the following (Secs. III E and III F) we will provide more detailed evidence for the spin-glass magnetism in Na-birnessite.

Fitting of $\chi(T)$ for Na-birnessite on the basis of the Curie-Weiss law $\chi = C/(T - \theta_{cw})$ is presented in the inset of Fig. 9. The derived values provide an estimate for the paramagnetic effective moment, $\mu_{eff} = 3.401(2)\,\mu_B$ and the Weiss temperature, $\theta_{cw} = -64.28(1)$ K. It is intriguing to analyze how the μ_{eff} for Na-birnessite is justified in view of the formal spin-only effective moments of Mn^{3+} (d^4) in its low-spin ($t_{2g}^4 e_g^0$; $S = 1$; $2.83\,\mu_B$) and high-spin ($t_{2g}^3 e_g^1$; $S = 2$; $4.9\,\mu_B$) configurations, as well as that of Mn^{4+} ($t_{2g}^3 e_g^0$; $S = 3/2$; $3.87\,\mu_B$). For example, in the chemically related $Na_{0.7}MnO_2$ the effective moment was estimated at $4.77\,\mu_B$ ($\theta_{cw} = -411$ K), closely resembling Mn^{3+} in a high-spin

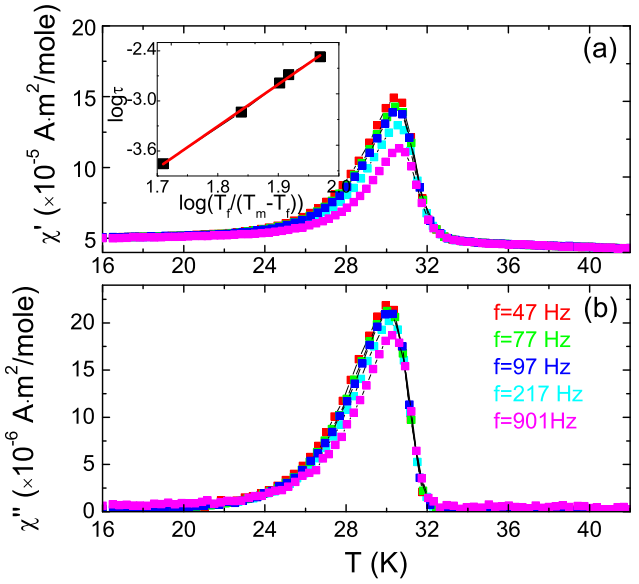

FIG. 10. Real (χ') and imaginary (χ'') parts of the ac susceptibility versus temperature at five different frequencies, under an ac drive field 0.3 mT. Inset: Power-law scaling analysis of the frequency dispersion of the real part χ' (T) peak temperature position.

state [43]. The μ_{eff} for Na-birnessite, on the other hand, may be attributed to a combination of two available valence states for the manganese cations, whose ratio Mn^{4+}/Mn^{3+} has been estimated as ~0.98 (Supplemental Material, S2) [44]. The literature reports suggest that when the Mn^{4+}/Mn^{3+} ratio is above a critical value of 0.4–0.5 [45], Mn^{3+} ions prefer the low-spin state; a case that appears to hold also for Na-birnessite. The unusual low-spin Mn^{3+} state has also been predicted by DFT and confirmed by magnetic susceptibility studies on Cr-doped rhombohedral $LiMnO_2$ ($\mu_{eff} = 2.97\,\mu_B$) [46]. Moreover, its occurrence in closely related porous manganese oxide octahedral sieves [47] has been claimed to emerge from the suppression of the Jahn-Teller distortion caused by the influence of higher valence cations such as Mn^{4+}. It is worth noting that in the parent oxide α-$NaMnO_2$, which is not a mixed valent compound, the Jahn-Teller active Mn^{3+} cations adopt the high-spin state alone [1], with antiferromagnetic long-range order at low temperatures. In view of the above, Na-birnessite and its chemically related dioxides, $Na_{0.7}MnO_2$ (hexagonal) [43] and α-$K_{0.087}MnO_2$ (tetragonal) [48], seem to support both site disorder (Mn^{3+} and Mn^{4+} mixture) induced by substoichiometry in the interlayer sites as well as frustration due to the underlying triangular sublattice that have both been claimed as the microscopic features central to the emerging spin-glass-like phase transitions.

E. Dynamic magnetic susceptibility

The transition to the spin-glass state is a dynamical process. Taking this into account, the signature for glassiness is derived and affirmed by ac magnetic susceptibility experiments. Figure 10 shows the real $\chi'(T)$ and imaginary $\chi''(T)$ parts of the susceptibility measured at five frequencies ($f = 47$, 77, 97, 217, 901 Hz) upon a ZFC mode under a 0.3-mT ac driving field. There are two notable characteristics. First, the peak observed in both the real and the imaginary parts of the magnetic susceptibility decreases with increasing frequency. Second, the frequency-dependent transition temperature, T_f, shifts to higher values as the frequency increases, similarly with the magnetic dynamics of other known spin-glass systems, such as, for example, the $Ge_{1-x}Mn_x$ [49] or the $La(Fe_{1-x}Mn_x)_{11.4}Si_{1.6}$ compounds [50]. In view of this, quantifying the frequency shift of the T_f, measured as the relative variation of $\chi'(T)$ peak-temperature position per frequency ($\omega = 2\pi f$) decade

$$K = \frac{\Delta T_f}{T_f \Delta(\log \omega)} \tag{1}$$

provides some phenomenological description on the strength of interactions and offers a good criterion for distinguishing a spin-glass behavior from that of a superparamagnet. This is known as the Mydosh parameter [42,51], which for Na-birnessite yields $K \sim 0.007$. It is worth noting that K falls in the range expected for spin glasses ($0.005 < K < 0.06$) [42,52–54] and is comparable with those values obtained for the prototypical, cooperative spin glasses of CuMn (0.005) [42] and AgMn (0.006) [42]. On the contrary, K for superparamagnets is an order of magnitude larger, varying from 0.1 to 0.3 on gradual blocking of moments [51]; for example, $K = 0.28$ for the α-$(Ho_2O_3)(B_2O_3)$ superparamagnet [42]. Therefore, the estimated Mydosh parameter excludes the scenario of the superparamagnetism for Na-birnessite.

It is well accepted though to verify the spin fluctuations and their strength by evaluating the frequency dispersion of the $\chi'(T)$ maximum [55]. The description of the latter by the available phenomenological laws (vide infra) evaluates the temperature dependence of the spin relaxation time τ, which, in turn, provides information on the underlined dynamics. In view of these, the Arrhenius law is utilized to describe weakly or noninteracting magnetic moments [42]:

$$\tau = \tau_o \exp\left(\frac{E_a}{k_B T}\right), \tag{2}$$

where E_a is the activation energy determined by the energy needed to exit out of a local potential well [56], τ_o is the "attempt" time [55,56], and T stands for the frequency dependent $\chi'(T)$ peak-temperature position, T_m from here onwards. However, the analysis on the basis of the Arrhenius law (Supplemental Material, S3) [44] resulted in physically unreasonable parameters, namely $\tau_o \sim 10^{-151}$ s ($\pm 10^{-159}$ s) and $\frac{E_a}{k_B} = 10254(567)$ K (Supplemental Material, Fig. S3) [44]. This failure adds further support to the argument that the spin dynamics in Na-birnessite is not dictated by superparamagnetic blocking of spins, but, instead, magnetic moments with elevated strength of interactions may come into play. For this, the Vogel-Fulcher law for intermediate strength interactions may be another appropriate candidate phenomenological description of spin fluctuations [57]:

$$\tau = \tau_o \exp\left(\frac{E_a/k_B}{T_m - T_f}\right), \tag{3}$$

where T_m is the frequency-dependent peak temperature for the real part of $\chi'(T)$, and T_f is the spin-glass freezing temperature that corresponds to a qualitative estimate of the

intersite interaction energy strength. However, the best fit from the Vogel-Fulcher analysis resulted in $T_f = 29.64$ K, $\frac{E_a}{k_B} = 2.09(1)$ K, and an attempt time, $\tau_o = 5.09 \times 10^{-6}$ ($\pm 1.02 \times 10^{-6}$ s) (Supplemental Material, Fig. S4) [44], unreasonably long for the material's nature. This τ_0 falls in the range expected for superspin glasses ($\sim 10^{-6}$ s) entailing magnetic nanoparticles [58,59] with dipole-dipole interactions instead of the shorter spin-flip times (10^{-9}–10^{-13} s) [42] anticipated for bulk systems with atomic Mn^{3+}/Mn^{4+} magnetic moments.

The inadequacy of both Arrhenius and Vogel-Fulcher laws to describe the collective spin-freezing close to T_f led us to infer that even stronger magnetic interactions may govern the spin dynamics in the Na-birnessite compound and are the likely reason for the observed deviations from the phenomenology described above. The dynamics of a spin-glass system with strong underlying magnetic interactions is in this case adequately described by the dynamic scaling theory [60]. This approach, based on the standard theory for the dynamical slowing down of spin dynamics near the freezing point T_f, considers a divergence of the relaxation time ($\tau = 1/\omega$) at a finite temperature (T_f), which can be described by the following critical power law:

$$\tau = \tau_o \left(\frac{T_f}{T_m - T_f} \right)^{z\nu}, \tag{4}$$

where τ_o is the characteristic attempt time that corresponds to the time needed for a single spin to undergo a transition from the paramagnetic to the frozen spin-glass state, T_m is the frequency-dependent $\chi'(T)$ peak-temperature position, and T_f is the static spin-glass transition temperature (equivalent to the freezing temperature when $f \to 0$), while the critical exponent, $z\nu$, has acceptable values between 4 and 12 for typical strongly interacting spin glasses [42].

The power-law scaling analysis of the frequency dispersion of the $\chi'(T)$ maximum is presented as a linear fit [61] in the inset of Fig. 10(a). The value of T_f has been adjusted manually in order to obtain the best linear fit in the $\log(\tau)$ versus $\log[T_f/(T_m - T_f)]$ plot, while the $z\nu$ and τ_o were derived from the least-squares fitting (Supplemental Material, S4) [44]. The best fit for Na-birnessite yielded the following quantities: $T_f = 29.64$ K, $\tau_o = 4.38 \times 10^{-13}$ ($\pm 0.49 \times 10^{-13}$) s, and $z\nu = 5.0(1)$. Previous investigations have suggested that some variation of these dynamic critical scaling parameters may infer materials of differing spin dimensionality [62–64]. For example, short-range insulating spin glasses, such as $Fe_{0.5}Mn_{0.5}TiO_3$, having Ising character and the Heisenberg-like (isotropic) $CdCr_{1.7}In_{0.3}S_4$, present a $z\nu = 10.5$ and $z\nu = 7$, respectively, whereas the characteristic attempt times of spin flip may be much larger than 10^{-12} s for the former and smaller than that for the latter. The aforementioned analysis of the temperature shift of the ac susceptibility cusp with the frequency (ω), together with the evidence for irreversibility (bifurcation) in the dc susceptibility, corroborate that Na-birnessite can be thought of as a magnetic system that resembles the cooperative behavior of other archetypical spin glasses (cf. CuMn, $z\nu = 5.5$ and $\tau_o \sim 10^{-12}$ s) [42,62,65].

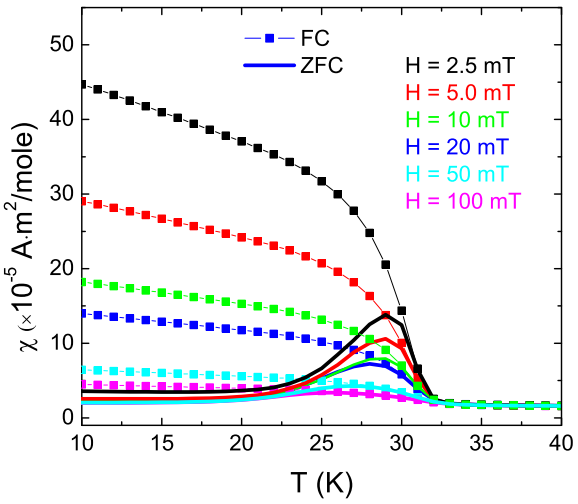

FIG. 11. Field-dependence of the ZFC-FC dc magnetic susceptibility of the Na-birnessite measured under magnetic fields ranging from 2.5 to 100 mT. The "cusp" at 29 K is eliminated as the external magnetic field is increased.

F. Field dependence of magnetic susceptibility

In order to further investigate the low-temperature transition and bearing in mind that in a spin glass the susceptibility cusp is very sensitive to an external applied magnetic field, $\chi(T)$ was studied under such a stimulus. Edwards and Anderson [66] predicted that the susceptibility field-dependent transition cusps become smeared out even under low magnetic fields. Indeed, this phenomenon is confirmed for Na-birnessite. Figure 11 presents the ZFC-FC $\chi(T)$ data measured at magnetic fields up to 100 mT. The sharpness of the transition is smeared out when the field is increased progressively ($\sim$20 mT) until it becomes almost flat for fields of $\sim$100 mT. Similar behavior has been observed in a number of magnetic systems that undergo a spin-glass freezing, such as the perovskites $La_{0.5}Sr_{0.5}CoO_3$ [39] and $Eu_{0.58}S_{0.42}MnO_3$ [67], as well as in chemically diverse intermetallic compounds, such as $PrRuSi_3$ [68]. In addition, the transition temperature, T_f, is shifted to lower values as the external magnetic field increases. A possible phase diagram for the crossover between paramagnetic and glassy states can then be roughly sketched (Fig. 12). This dc field dependence of $T_f(H)$ [39,50,69] has been assessed on the basis of the mean-free model of Sherrington and Kirkpatrick [70]:

$$\frac{T_f(0) - T_f(H)}{T_f(0)} \propto H^{\delta}. \tag{5}$$

It broadly represents a critical line that defines the onset of irreversibility when entering the spin-glass state in the H-T phase space. In a Heisenberg (isotropic) spin system, the transition occurs along the Gabay-Toulouse [71] (GT) line for $\delta = 2$ [72], while for an Ising type, the transition occurs along the de Almeida-Thouless [73] (AT) line for values of $\delta = 2/3$. From the least-square fitting (inset, Fig. 12), Na-birnessite appears to follow the AT-like line of $H^{2/3}$, instead of GT line (Supplemental Material, S6) [44] for isotropic spins, a behavior that might have been inferred by the analysis of the dynamical scaling exponent ($z\nu$) and the Mydosh parameter.

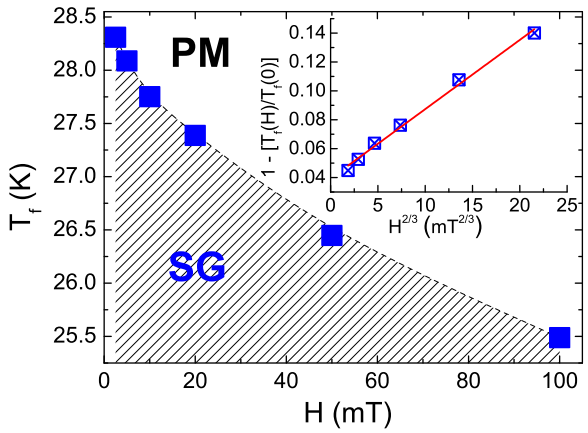

FIG. 12. The magnetic field dependence of the freezing temperature (T_f) in the Na-birnessite depicts a relevant phase-diagram for the transition between the PM (paramagnetic) and SG (spin glass) states. Inset: Least square fit of the reduced temperature in the de Almeida-Thouless mean-free model [Eq. (5)].

This likely discrepancy may be reconciled by claiming the role of weak, random anisotropy (e.g., Dzyaloshinsky-Moriya, single-ion, etc.) that is usually present in real systems [74,75]. Mean-field calculations have predicted that when anisotropic interactions are present, an otherwise Heisenberg spin-glass exhibits an Ising-like behavior in the low-field limit [76,77]. This has been verified experimentally in spin glasses of diverse chemical nature, ranging from the archetype metallic Ruderman-Kittel-Kasuya-Yosida (RKKY) CuMn [78] system to short-range interacting, insulating $CdCr_{1.7}In_{0.3}S_4$ [79] and semiconducting $Cd_{0.62}Mn_{0.38}Te$ [80] compounds. The present experimental data in Na-birnessite could suggest that anisotropic interactions should be taken into account, but, on the other hand, can also imply that such conventional experiments may not be sufficiently sensitive [75] to the freezing of transverse spin degrees of freedom that are identifying features of Heisenberg spin glasses, consistent with a transition line of the GT type. Nevertheless, further experimental evidence from the critical behavior in the field-temperature phase diagram and the associated critical dynamics (e.g., isothermal time decay of AC susceptibility) may be required in order to verify the dimensionality of the spin interactions in the system under study.

G. Interactions in Related Manganese Dioxides

An interesting reference system, due to its chemical affinity, is the hexagonal $Na_{0.7}MnO_2$ ($P6_3/mmc$; $a = 2.811$ Å, $c = 11.118$ Å) layered derivative that has been identified to undergo a spin-glass transition at $T_f \leqslant 39$ K [43] due to random distribution of the Mn^{3+}/Mn^{4+} cations in a frustrated triangular lattice topology. Consequently, glassiness develops and reflects on the dc susceptibility, with common features between the two materials pertaining to the ZFC-FC divergence in $\chi(T)$, the elimination of the ZFC-FC $\chi(T)$ maximum upon the application of moderate external magnetic fields ($H < 500$ mT), and the comparable Mydosh parameter, which was calculated as $K = 0.004$ for $Na_{0.7}MnO_2$. Interestingly, the bifurcation of the ZFC/FC susceptibilities below T_f indicates weakly coupled ferromagnetic species for both, with a comparable coercive field of about 0.1 T in the 5 to 10 K region (Fig. S5 and Fig. 4 of Ref. [43]). To rationalize this, the different degree of Mn^{3+}:Mn^{4+} disproportionation in the two systems needs to be considered, namely 0.86:0.14 for $Na_{0.7}MnO_2$ versus 0.51:0.49 for Na-birnessite (Supplemental Material, S2) [44]. Although a rigorous evaluation of the relative magnitude of interactions between any pair of Mn cations is difficult given the large number of individual microscopic processes involved in the magnetic exchange pathways, one expects that the increased abundance of Mn^{4+} states in Na-birnessite will enhance ferromagnetic interactions (as Mn^{4+}-O-Mn^{4+} 90° superexchange is ferromagnetic) [81], in analogy to the closely related layered $Na_{5/8}MnO_2$ [23]. Consequently, with the weight of the interactions likely shifted to ferromagnetic-like (against antiferromagnetic) correlations, the reduction in the Curie-Weiss temperature for Na-birnessite is also anticipated (i.e., −64 K vs. −411 K for $Na_{0.7}MnO_2$). The material offers a test-bed to probe subtle details of competing processes in multivalent Mn systems, thus going beyond cooperative magnetism and possibly into emerging rechargeable battery technologies. In view of the latter, electron-driven (Jahn-Teller) lattice transformations met in Na_xMnO_2 derivatives deserve to be studied as a reason to understand how to avoid impairing [23,82,83] the electrochemical properties of candidate layered oxides for sodium-ion rechargeable cathodes.

On the origin of the spin-glass state in Na-birnessite

In chemically related dioxides, such as $Na_{0.7}MnO_2$ and α-$K_{0.087}MnO_2$, with frustrated triangular Mn topology, alkali metal off-stoichiometry in the interlayer sites imposes disorder in the manganese sublattice by random generation of Mn^{3+} and Mn^{4+} states (site disorder) [43,48]. This promotes bond disorder (i.e., the sign of the exchange interaction between nearest neighbors may flip at random from AFM to FM and vice versa) and therefore raises frustration [84]. In view of the latter, it is useful to highlight some of the observed microscopic characteristics of the Na-birnessite structure. The abore-mentioned avenues for site disorder (and frustration) in the compound under the present study would be enhanced due to possible vacancies in the MnO_6 layers. For example, the Mn vacancies, whether attributed to the Mn^{3+} or Mn^{4+} cations, would result in the disruption of the long-range periodicity of the magnetic interactions. Imperfections of the crystal structure and specifically, stacking faults were indeed revealed by the HRTEM experiments [Fig. 2(c)]. Planar defects of this type have a significant impact as they alter the exchange pathways, the relative number and strength of exchange interactions, as well as the type of the magnetic coupling (AFM or FM) [3]. Under these conditions the development of various competing exchange interactions and their interplay would give rise to frustration. An empirical way to estimate the degree of frustration is to calculate the ratio $f = -\theta_{cw}/T_N$, where T_N is a temperature at which the system would order cooperatively. The values of $f > 1$ imply that the material is magnetically frustrated [85]. Regarding the compound under study, $f = 2.21$ (with $\theta_{cw} = -64.28$ K and $T_N = 29$ K), a value in accord with the previous arguments.

Although the triangular in-plane lattice topology triggers magnetic frustration *per se*, the simultaneous presence of Mn^{3+}/Mn^{4+} cations that are randomly distributed within the MnO_6 layers is an additional avenue generating competing exchange interactions, in turn promoting spin frustration and collective spin-glass freezing in the hydrated variant of the α-$NaMnO_2$ antiferromagnet.

IV. CONCLUSIONS

In summary, we have shown a paradigm where facile, hydration preparative routes to layered sodium manganese dioxides have driven significant alteration of the crystal structure, leading to fundamental changes in the electronic character and the magnetic state, therefore opening prospects for enhanced functional behavior. Specifically, the insertion of H_2O molecules in the interlayer spacing of the two-dimensional frustrated antiferromagnet α-$NaMnO_2$ leads to the formation of the $Na_{0.36}MnO_2 \cdot 0.2H_2O$ derivative with enhanced MnO_6-layer separation and mixed valency that offers favorable redox attributes for technologically useful, rechargeable battery cathode materials. From a fundamental point of view, the intercalation of water in α-$NaMnO_2$ has a dramatic impact on the antiferromagnetic ground state of the parent compound ($T_N = 45$ K). Na-birnessite is shown to enter a cooperative spin-frozen state, at $T_f = 29$ K, where the critical dynamics of strongly interacting spins is governed by the divergence of their relaxation times. This is in agreement with the power-law scaling theory that dictates the magnetic dynamics before the collective spin-glass freezing. The variation in the magnetic response, imposed by the structural transformation and the chemically driven in-plane defect environment due to crystal H_2O, highlight the critical impact of topology and site disorder on frustrated magnetism.

ACKNOWLEDGMENTS

This research has in part been carried out in the framework of Heracleitus II project (Grant No. 349309 WP1.56) cofinanced by the Ministry of Education & Religious Affairs, Greece and the European Social Fund, European Union (Operational Programme: Education and Lifelong Learning, NSRF 2007–2013). Part of this work was performed in the framework of the PROENYL research project, Action KRIPIS, Project No. MIS-448305 (2013SE01380034), cofinanced by the General Secretariat for Research and Technology, Ministry of Education, Greece, and the European Regional Development Fund (Sectoral Operational Programme: Competitiveness and Entrepreneurship, NSRF 2007–2013)/European Commission. We acknowledge the support of the National Institute of Standards and Technology, U.S. Department of Commerce, in providing the neutron research facilities used in this work. A.T. acknowledges financial support from the Federal Ministry for Education and Research through the Sofja Kovalevskaya Award of Alexander von Humboldt-Stiftung.

[1] M. Giot, L. C. Chapon, J. Androulakis, M. A. Green, P. G. Radaelli, and A. Lappas, Phys. Rev. Lett. **99**, 247211 (2007).
[2] J. B. Goodenough, Phys. Rev. **100**, 564 (1955).
[3] A. M. Abakumov, A. Tsirlin, I. Bakaimi, G. Van Tendeloo, and A. Lappas, Chem. Mater. **26**, 3306 (2014).
[4] S. T. Wong and S. Cheng, Inorg. Chem. **31**, 1165 (1992).
[5] R. Sen, A. Govindaraj, K. Suenaga, S. Suzuki, H. Kataura, S. Iijima, and Y. Achiba, Chem. Phys. Lett. **340**, 242 (2001).
[6] A. R. Armstrong and P. G. Bruce, Nature **381**, 499 (1996).
[7] I. Kruk, P. Zajdel, W. van Beek, I. Bakaimi, A. Lappas, C. Stock, and M. A. Green, J. Am. Chem. Soc. **133**, 13950 (2011).
[8] J. P. Parant, R. Olazcuaga, M. Devalette, C. Fouassier, and P. Hagenmuller, J. Solid State Chem. **3**, 1 (1971).
[9] J. Billaud, R. J. Clement, R. A. Armstrong, J. Canales-Vazquez, P. Rozier, C. Grey, and P. Bruce, J. Am. Chem. Soc. **136**, 17243 (2014).
[10] T. Kijima, *Inorganic and Metallic Nanotubular Material: Recent Technologies and Applications, Topics in Applied Physics*, (Springer, Berlin, 2010), p. 74.
[11] M. H. Rossouw, D. C. Liles, and M. M. Thackeray, J. Solid State Chem. **104**, 464 (1993).
[12] Q. Feng, L. Liu, and K. Yanagisawa, J. Mater. Sci. Lett. **19**, 1567 (2000).
[13] D. C. Golden, C. C. Chen, and J. B. Dixon, Clays and Clay Minerals **35**, 271 (1987).
[14] J. Luo and S. L. Suib, J. Phys. Chem. B **101**, 10403 (1997).
[15] O. Prieto, M. Del Arco, and V. Rives, J. Mater. Sci. **38**, 2815 (2003).
[16] B. Lee, S. C. Yoon, H. R. Lee, K. Y. Chung, B. W. Cho, and S. Y. Oh, Sci. Rep. **4**, 6066 (2014).
[17] K. W. Nam, S. Kim, E. Yang, Y. Jung, E. Levi, D. Aurbach, and J. W. Choi, Chem. Mater. **27**, 3721 (2015).
[18] Q. Feng, H. Kanoh, Y. Miyai, and K. Ooi, Chem. Mater. **7**, 1226 (1995).
[19] Q. Feng, H. Kanoh, and K. Ooi, J. Mater. Chem. **9**, 319 (1999).
[20] Y. U. Jeong and A. Manthiram, J. Solid State Chem. **156**, 331 (2001).
[21] A. Zorko, O. Adamopoulos, M. Komelj, D. Arcon, and A. Lappas, Nat. Commun. **5**, 3222 (2014).
[22] S. Hirano, R. Narita, and S. Naka, Matt. Res. Bull. **19**, 1229 (1984).
[23] X. Li, X. Ma, D. Su, L. Liu, R.Chisnell, S. Ping Ong, H. Chen, A. Toumar, J.-C. Idrobo, Y. Lei, J. Bai, F. Wang, J. W. Lynn, Y. B. Lee, and G. Ceder. Nat. Mater. **13**, 586 (2014).
[24] H. T. Zhu, J. Luo, H. X. Yang, J. K. Liang, G. H. Rao, J. B. Li, and Z. M. Du, J. Phys. Chem. C **112**, 17089 (2008).
[25] K. S. Abou-El-Sherbini, M. H. Askar, and R. Schollhorn, Solid State Ionics **150**, 407 (2002).
[26] Certain commercial equipment, instruments, or materials are identified in this document. Such identification does not imply recommendation or endorsement by the National Institute of Standards and Technology nor does it imply that the products identified are necessarily the best available for the purpose.
[27] J. Verbeeck and S. Van Aert, Ultramicroscopy **101**, 207 (2004).

[28] L. Espinal, W. Wong-Ng, J. A. Kaduk, A.J. Allen, C. R. Snyder, C. Chiu, D. W. Siderius, L. Li, E. Cockayne, A. E. Espinal, and S. Suib, J. Am. Chem. Soc. **134**, 7944 (2012).

[29] H. Tan, J. Verbeeck, A. Abakumov, and G. Van Tendeloo, Ultramicroscopy **116**, 24 (2012).

[30] T. Riedl, T. Gemming, and K. Wetzig, Ultramicroscopy **106**, 284 (2006).

[31] P. A. van Aken and B. Liebscher, Phys. Chem. Miner. **29**, 188 (2002).

[32] J. Graetz, C. C. Ahn, H. Ouyang, P. Rez, and B. Fultz, Phys. Rev. B **69**, 235103 (2004).

[33] R. D. Leapman and L. A. Grunes, Phys. Rev. Lett. **45**, 397 (1980).

[34] T. Riedl, T. Gemming, W. Gruner, J. Acker, and K. Wetzig, Micron **38**, 224 (2007).

[35] S. Bedanta and W. Kleemann, J. Phys. D: Appl. Phys. **42**, 013001 (2009).

[36] X. Yang, J. Makita, Z. Liu, K. Sakane, and K. Ooi, Chem. Mater. **16**, 5581 (2004).

[37] C. Stock, L. C. Chapon, O. Adamopoulos, A. Lappas, M. Giot, J. W. Taylor, M. A. Green, C. M. Brown, and P. G. Radaelli, Phys. Rev. Lett. **103**, 077202 (2009).

[38] A. Zorko, J. Kokalj, M. Komelj, O. Adamopoulos, H. Luetkens, D. Arcon, and A. Lappas, Sci. Rep. **5**, 9272 (2015).

[39] D. N. H. Nam, K. Jonason, P. Nordblad, N. V. Khiem, and N. X. Phuc, Phys. Rev. B **59**, 4189 (1999).

[40] K. Singh, A. Maignan, C. Simon, V. Hardy, E. Pachoud, and C. Martin, J. Phys.: Condens. Matter **23**, 126005 (2011).

[41] G. C. DeFotis, G. S. Coker, J. W. Jones, C. S. Branch, H. A. King, J. S. Bergman, S. Lee, and J. R. Goodey, Phys. Rev. B **58**, 12178 (1998).

[42] J. A. Mydosh, *Spin Glasses:An Experimental Introduction* (Taylor & Francis, London, 1993), p. 67, p. 70-71.

[43] L. B. Luo, Y. G. Zhao, G. M. Zhang, S. M. Guo, Z. Li, and J. L. Luo, Phys. Rev. B **75**, 125115 (2007).

[44] See Supplemental Material at http://link.aps.org/supplemental/10.1103/PhysRevB.93.184422 for Na-birnessite for figures from TEM studies (S1), estimation of the ratio Mn^{3+}:Mn^{4+} (S2), ac susceptibility data analyses: Arrhenius and Vogel-Fulcher laws (S3) and the power law (S4), the hysterisis loop at 5 K (S5), and the Gabay-Toulouse analysis (S6).

[45] D. Reinen, U. Kesper, and D. Belder, J. Solid State Chem. **116**, 355 (1995).

[46] Z. F. Huang, F. Du, C.-Z. Wang, D.-P. Wang, and G. Chen, Phys. Rev. B **75**, 054411 (2007).

[47] X. F. Shen, Y. S. Ding, J. Liu, Z. H. Han, J. I. Budnick, W. A. Hines, and S. L. Suib, J. Am. Chem. Soc. **127**, 6166 (2005).

[48] J. Luo, H. T. Zhu, F. Zhang, J. K. Liang, G. H. Rao, J. B. Li, and Z. M. Du, J. Appl. Phys. **105**, 093925 (2009).

[49] C. Jaeger, C. Bihler, T. Vallaitis, S. T. B. Goennenwein, M. Opel, R. Gross, and M. S. Brandt, Phys. Rev. B **74**, 045330 (2006).

[50] F. Wang, J. Zhang, Y.-f. Chen, G.-j. Wang, J.-r. Sun, S.-y. Zhang, and B.-g. Shen, Phys. Rev. B **69**, 094424 (2004).

[51] J. A. Mydosh, Rep. Prog. Phys. **78**, 052501 (2015).

[52] C. A. M. Mulder, A. J. van Duyneveldt, and J. A. Mydosh, Phys. Rev. B **23**, 1384 (1981).

[53] S. Harikrishnan, C. M. N. Kumar, H. L. Bhat, S. Elizabeth, U. K. Roessler, K. Doerr, S. Roessler, and S. Wirth, J. Phys.: Condens. Matter **20**, 275234 (2008).

[54] I. M. Siouris, J. Magn. Magn. Mater. **309**, 222 (2007).

[55] A. Kostopoulou, K. Brintakis, M. Vasilakaki, K. N. Trohidou, A. P. Douvalis, A. Lascialfari, L. Manna, and A. Lappas, Nanoscale **6**, 3764 (2014).

[56] W. M. Saslow, Phys. Rev. B **37**, 676 (1988).

[57] S. Shtrikman and E. P. Wohlfarth, Phys. Lett. A **85**, 467 (1981).

[58] C. Djurberg, P. Svedlindh, P. Nordblad, M. F. Hansen, F. Bodker, and S. Morup, Phys. Rev. Lett. **79**, 5154 (1997).

[59] O. Petracic, W. Kleeman, C. Binek, G. N. Kakazei, Y. G. Pogorelov, J. B. Sousa, S. Gardoso, and P. P. Freitas, Phase Transit. **75**, 73 (2002).

[60] J. Lago, S. J. Blundell, A. Eguia, M. Jansen, and T. Rojo, Phys. Rev. B **86**, 064412 (2012).

[61] Y. Bréard, V. Hardy, B. Raveau, A. Maignan, H. J. Lin, L. Y. Jang, H. H. Hsieh, and C. T. Chen, J. Phys.: Condens. Matter **19**, 216212 (2007).

[62] V. Dupuis, E. Vincent, J. P. Bouchaud, J. Hammann, A. Ito, and H. A. Katori, Phys. Rev. B **64**, 174204 (2001).

[63] P. E. Jonsson, H. Yoshino, P. Nordblad, H. Aruga Katori, and A. Ito, Phys. Rev. Lett. **88**, 257204 (2002).

[64] I. A. Campbell, Phys. Rev. B **37**, 9800 (1988).

[65] A. Maignan, C. Martin, K. Singh, C. Simon, O. I. Lebedev, and S. Turner, J. Solid State Chem. **195**, 41 (2012).

[66] S. F. Edwards and P. W. Anderson, J. Phys. F **5**, 965 (1975).

[67] A. Sundaresan, A. Maignan, and B. Raveau, Phys. Rev. B **55**, 5596 (1997).

[68] V. K. Anand, D. T. Adroja, A. D. Hillier, J. Taylor, and G. André, Phys. Rev. B **84**, 064440 (2011).

[69] D. X. Li, S. Nimori, Y. Shiokawa, A. Tobo, H. Onodera, Y. Haga, E. Yamamoto, and Y. Onuki, Appl. Phys. Lett. **79**, 4183 (2001).

[70] D. Sherrington and S. Kirkpatrick, Phys. Rev. Lett. **35**, 1792 (1975).

[71] M. Gabay and G. Toulouse, Phys. Rev. Lett. **47**, 201 (1981).

[72] K. H. Fischer and J. A. Hertz, *Spin Glasses* (Cambrigde University Press, New York, 1991), p. 171.

[73] J. R. L. Almeida and D. J. Thouless, J. Phys. A: Math. Gen **11**, 983 (1978).

[74] A. Fert and P. M. Levy, Phys. Rev. Lett. **44**, 1538 (1980).

[75] N. de Courtenay, A. Fert, and I. A. Campbell, Phys. Rev. B **30**, 6791 (1984).

[76] G. Kotliar and H. Sompolinsky, Phys. Rev. Lett. **53**, 1751 (1984).

[77] K. H. Fischer, Z. Phys. B: Condens. Matter **60**, 151 (1985).

[78] G. G. Kenning, D. Chu, and R. Orbach, Phys Rev. Lett. **66**, 2923 (1991).

[79] F. Lefloch, J. Hammann, M. Ocio, and E. Vincent, Physica B Condens. Matter **203**, 63 (1994).

[80] F. Bernardot and C. Rigaux, Phys Rev. B **56**, 2328 (1997).

[81] J. B. Goodenough, Phys. Rev. **117**, 1442 (1960).

[82] M. M. Thackeray, Prog. Solid State Chem. **25**, 1 (1997).

[83] Z. Lu, D. D. MacNeil, and J. R. Dahn, Electrochem. Solid State **4**, A191 (2001).

[84] R. Moessner and A. P. Ramirez, Phys. Today **59**, 24 (2006).

[85] A. P. Ramirez, Annu. Rev. Mater. Sci. **24**, 453 (1994).